Appl Phys B (2008) 93: 69–78
DOI 10.1007/s00340-008-3212-2

Applied Physics B
Lasers and Optics

Plasmon coupling in binary metal core–satellite assemblies

D.S. Sebba · T.H. LaBean · A.A. Lazarides

Received: 28 June 2008 / Revised version: 29 August 2008 / Published online: 13 September 2008

Abstract Controlled plasmon coupling is observed in nanoparticle assemblies composed of 20 nm silver 'satellite' nanoparticles tethered by reconfigurable duplex DNA linkers to a 50 nm gold 'core' particle. The assemblies incorporate silver nanoparticle–oligonucleotide conjugates prepared using a new conjugation method in which the recognition strand is anchored by a 10 base pair, double strand spacer that presents adjacent 3'- and 5'-thiols to the silver surface. Reconfiguration of the DNA linkers from a compact to an extended state results in decreased core–satellite coupling and a blue-shift in the gold core plasmon resonance. The structural basis for the observed resonance modulation is investigated through simulation of the scattering spectra of binary assemblies with various core–satellite separations. Additional simulations of core–satellite assemblies composed of gold satellite particles bound to silver cores and of assemblies composed entirely of silver particles are used to clarify the dependence of the coupling response on the composition of the components and their distribution within the assembly.

PACS 81.07.-b · 82.70.Dd · 81.16.Dn · 87.85.J · 87.85.Qr

1 Introduction

Metal nanoparticles support localized surface plasmon resonances that are sensitive to particle size, shape, composition [1–3], and proximity to other resonant particles [4, 5] and materials [6–10]. The modulation of the localized surface plasmon resonance that occurs when plasmons are delocalized over multiple particles has motivated the development of nanoscale sensing structures that exploit the strong distance dependence of interparticle plasmon coupling. Multicomponent nanostructures developed for molecular detection applications have been assembled under the direction of biomolecular linkers such as oligonucleotides [4, 11–13] and proteins [14–16], and have ranged in extent from networks incorporating thousands of particles [4, 12] to structures comprised of as few as two particles [17, 18].

Many of the reported biomolecule-linked metal nanoparticle structures have been composed of particles of like composition, and, in particular, gold particles. Self-assembled structures, typically, support a plasmon resonance that is red-shifted and broadened relative to the localized surface plasmon resonance of dispersed components [19]. However, nanoparticles composed of other metals such as silver, copper, and platinum also support localized surface plasmon resonances [2, 20, 21]. Silver particles are of particular interest [12, 22] because of the metal's low intrinsic loss, the property responsible also for its high conductivity.

Electronic supplementary material The online version of this article (http://dx.doi.org/10.1007/s00340-008-3212-2) contains supplementary material, which is available to authorized users.

D.S. Sebba · A.A. Lazarides (✉)
Department of Mechanical Engineering and Materials Science,
Duke University, Durham, NC 27708, USA
e-mail: anne.lazarides@duke.edu
Fax: +1-919-6605409

T.H. LaBean
Department of Chemistry, Duke University, Durham,
NC 27708, USA

T.H. LaBean
Department of Computer Science, Duke University, Durham,
NC 27708, USA

Reliable methods of forming stable DNA-functionalized silver nanoparticles have, until recently, proven to be elusive. Surface adsorption of thiolated oligonucleotides, a process used routinely to form gold particle conjugates [23], results in degradation of the silver surface [24] and produces conjugates of limited stability [12, 22]. Recently, silver particle stabilization has been demonstrated using multi-dentate ligands synthesized by coupling oligonucleotides to multiple disulfide-containing phosphoramidite units [25]. Stable DNA–silver nanoparticle conjugates have been used for ultrasensitive DNA detection [26], and may be useful in a variety of other applications where a strong plasmon signal is desirable.

A less widely recognized barrier to exploiting the distance-dependent properties of plasmon coupling within nanoparticle assemblies derives from the multiplicity of phenomena that lead to shifting of a plasmon resonance. In aggregates of like particles, band position is highly sensitive, not only to interparticle separation, but also to coordination number and aggregate size [27]. In samples with diverse components, particle aggregation may occur in response to many stimuli and result in aggregates of variable size supporting plasmons with a broad range of frequencies. A strategy that may facilitate detection of a specifically driven response is to use preassembled structures composed of a fixed number of particles that reproducibly support resonances within a narrow band of wavelengths.

Recently we have reported molecularly driven plasmon modulation in preformed, few particle assemblies linked by reconfigurable DNA, nanostructures [28]. That investigation was motivated by the potential of reconfigurable nanoparticle assemblies to provide control of plasmon coupling in a format that displays strong perturbation of the plasmon in response to molecular assembly, but avoids interpretive difficulties associated with uncontrolled aggregation. In the reported assemblies, multiple gold ‘satellite’ particles were tethered to a single gold ‘core’ particle by DNA nanostructure linkers, Fig. 1. The DNA nanostructures control interparticle separation and are responsive to target strands that modulate interparticle helix length, and thus, core–satellite separation. While, in general, plasmon perturbation that results from reconfiguration of core–satellite tethers in a gold particle assembly depends upon particle sizes and the number of satellites per core, for the specific structures investigated, perturbation depends upon variation in interparticle separation, and, in particular, core–satellite separation in the compact assembly state.

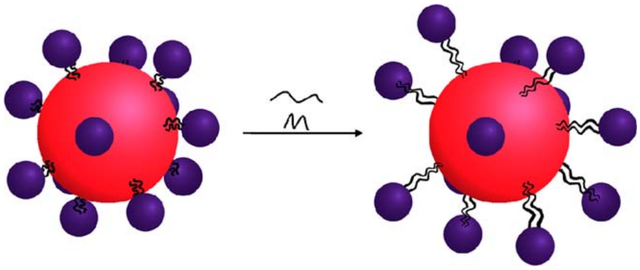

Fig. 1 Core–satellite expansion driven by tether reconfiguration

Here, we extend our investigation of controlled plasmon coupling to few particle assemblies composed of particles of unlike composition. Our goal is to characterize plasmon coupling in binary assemblies composed of unlike components. As in prior work with structures composed of like particles, we use a reconfigurable assembly of well-defined geometry that provides control of plasmon coupling in both configurations. Initially, we investigate DNA-linked structures composed of a small number of gold and silver nanoparticles, i.e. structures that support two distinct resonances associated with the two plasmonic components. Towards this end, we have developed a new approach to forming stable silver particle DNA conjugates, a method that involves assembly of readily available components in lieu of chemical synthesis of new derivatives. Particles are functionalized with a strand consisting of a recognition sequence and a thiolated A_{10} spacer that is partially hybridized to a thiolated T_{10} strand; thus, the DNA is anchored to the silver surface through a 10 base pair helix that presents both 3’- and 5’-thiols. To identify the properties of plasmon coupling unique to binary assemblies, we assemble gold and silver DNA conjugates into core satellite structures similar to those formed previously using core and satellite conjugates composed exclusively of gold [28].

We report solution phase assembly of gold core/silver satellite structures formed from nanoparticle–oligonucleotide conjugates linked together with reconfigurable double helical DNA tethers. First, we describe the formation of stable silver nanoparticle–oligonucleotide conjugates. Next, we demonstrate the synthesis of $\sim$100 nm binary assemblies formed by tethering the silver nanoparticle conjugates to 50 nm gold nanoparticle cores. Subsequently, we monitor the transformation of strongly coupled compact structures to larger, weakly coupled structures through reconfiguration of the DNA nanostructure tethers that link the silver satellite particles to gold cores. TEM is used to characterize the structural integrity of the reconfigured structures and visible scattering spectroscopy is used to monitor the effect on plasmon coupling of extension of the DNA tether. Following presentation of the data, we describe a model of assembly structure that incorporates core–satellite ratios observed in TEM and tether structures similar to, but slightly longer than, those used previously to link gold satellite particles to gold nanoparticle cores. Subsequently, we report the results of spectral simulations performed to confirm that the spectral properties observed following both satellite assembly and tether reconfiguration are consistent with the effects of plasmon coupling predicted by electrodynamic theory given the structural models. Finally, to clarify how plasmon coupling in binary nanoparticle structures depends upon the detailed distribution of material properties among assembly components, additional spectral simulations are reported. For a series of particle geometries loosely representative of those reported here for binary assemblies and reported previously for assemblies composed of gold particles, scattering spectra were calculated for four permutations of component properties, i.e. gold or silver satellites on gold or silver cores.

2 Materials and methods

2.1 Materials

50 nm gold colloid and silver colloid of nominal mean size between 15 and 25 nm were purchased from Ted Pella. Oligonucleotides were purchased from IDT DNA Technologies.

2.2 Preparation of DNA-functionalized nanoparticles

Gold colloid was functionalized with strand *b* (5'-SH-A_{10}-CGC ATT CAG GAT-3') using previously described methods [23]. To produce stable functionalized silver, colloid was exposed to equal amounts of oligonucleotide $b^*defe^*g\text{-}s$ (5'-SH-C_6-A_{10}-TCT CAA CTC GTA CGC ATG ATT GTT TTC AAT CAT GCG CGA AAG ATC CTG AAT GCG-3') and its partial complement s^* (5'-T_{10}-C_3-C_3-C_3-SH-3'). Strand $b^*defe^*g\text{-}s$ incorporates the oligonucleotide b^*defe^*g, a hairpin forming oligonucleotide used previously to functionalize colloidal gold [28], and an additional sequence, s^* (5'-SH-C_3-A_{10}), which, upon hybridization, forms a double helix that presents two thiols to the silver surface. The mixture was salt-aged over 48 h to a final concentration of 0.1 M NaCl, 10 mM phosphate buffered saline (PBS), and then washed at 9 k relative centrifugal force (rcf) for 12 min. The supernatant was washed at 12 k rcf for 14 min, and washed supernatant was included in the silver satellite solution and aged for another 48 h prior to use. These conjugates show minimal changes in their UV-visible extinction spectrum for 3–4 weeks (less than 5% decrease in amplitude, no signs of broadening, Supplementary Material Fig. S1), indicating that they are relatively stable and, within the time-frame of the work presented here, do not aggregate.

Silver colloid concentration was estimated to be 1.11 nM using an extinction coefficient, $\varepsilon_{400} = 4.83 \times 10^9\ \text{mol liter}^{-1}\,\text{cm}^{-1}$, derived by scaling extinction coefficients for 20 nm gold colloid [23] using the theoretical ratio of peak intensities for 20 nm gold and 20 nm silver colloid in water. Theoretical intensities were determined using Mie theory and dielectric functions [30, 31] corrected for nanoparticle size [32]. Functionalized silver colloid was imaged using TEM and found to be of size 20.5 ± 3.4 nm and mean in-plane aspect ratio 1.15 based upon 50 imaged particles. Further shape dispersity associated with the out-of-plane third dimension was not determined. Uncertainty in the silver concentration was significant due to the non-sphericity of the silver colloid and the use of an extinction ratio accurate for spheres. Indications of silver particle eccentricity were an 8 nm offset in peak location and a 36% broader width observed in the extinction spectrum relative to the peak and width of the simulated plasmon band calculated for a sphere and used to determine concentration.

2.3 Assembly of gold core/silver satellite structures

Cores (20 µL of 0.12 nM solution), satellites (100 µL of 1.11 nM solution), and buffer (700 µL), were mixed with short complement strand $m\text{-}d^*g^*$ (10 µL of 63.3 µM solution, 5'-TGA ATG AGC TTT CGT ACG AGT TGA GA-3'), heated to 52°C and allowed to cool to room temperature. Assemblies were reconfigured by adding $m^*\text{-}dg$ (13.5 µL of 90 µM solution, 5'-TCT CAA CTC GTA CGA AAG CTC ATT CA-3') and $d^*e^*f^*eg^*$ (13.5 µL of 90 µM solution, 5'-CTT TCG CGC ATG ATT GAA AAC AAT CAT GCG TAG GAG TTG AGA-3'). Final concentrations in the hairpin state were as follows: Cores—2.9 pM, satellites—0.134 nM, $m\text{-}d^*g^*$—0.76 µM. Final concentrations in the extended state were as follows: cores—2.8 pM, satellites—0.13 nM, $m\text{-}d^*g^*$—0.74 µM, $m^*\text{-}dg$—1.4 µM, $d^*e^*f^*eg^*$—1.4 µM.

2.4 Optical characterization

Ensemble scattering spectra were collected on a custom UV-visible spectrometer (On Line Instrument Systems) capable of collecting both transmitted and scattered light.

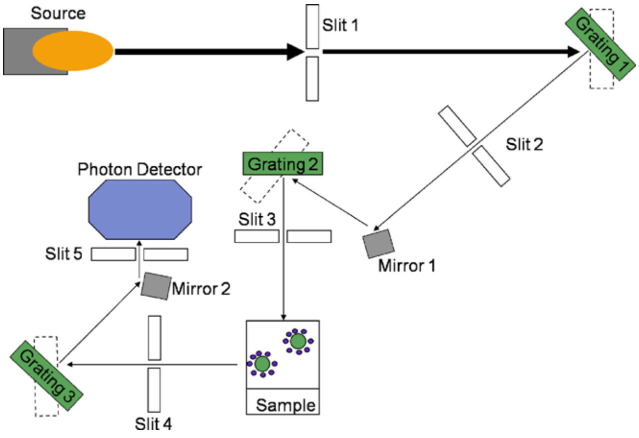

Fig. 2 Schematic of spectrometer. A double monochrometer controls spectral resolution of the incident light; elastically scattered light is selected by a single monochrometer

A schematic of the instrument in its scattering configuration is illustrated in Fig. 2. A 150 W Xenon lamp is used for illumination, and a double monochrometer (1200 lines, 450 blaze) selects the wavelength of light incident upon the sample. Scattered light is collected through a single monochrometer and detected by a trialkali photon counter optimized for red sensitivity (Electron Tubes, 9113WB80). Spectral resolution of the incident and scattered light are controlled by the width of the entrance and exit slits; in this work, 1.24 mm slits were used to provide a bandpass of 5 nm. Scattered light was collected at 0.75 nm within a wavelength range of 514.75 to 610 nm using a collection time of 2.55 s.

2.5 Transmission electron microscopy

Transmission electron microscopy (TEM) grids were prepared by pipetting a 10 μL drop of solution onto a grid and allowing it to sit for 2–4 min prior to wicking away liquid with a kimwipe. TEM imaging was performed on a Hitachi HF-2000 microscope operating at an accelerating voltage of 200 KeV.

2.6 Spectral simulations

Spectra were simulated using an electrodynamic, coupled multipole, T-matrix method [29] that provides a fully converged description of the delocalized modes supported by a cluster of spherical particles. The response of the cluster to an incident plane wave is determined by self-consistent solution of the linear combinations of modes excited at each particle in response to the local field equal to the superposition of the incident field and the fields of the other particles. The response of each sphere is determined using Mie coefficients following expansion of the local field at each particle in a sum of sphere-centered vector spherical harmonics. Transformations that translate harmonic modes between particles as required for solution of the coupled problem are determined by the cluster geometry and embedded in the T-matrix. Scattering spectra are evaluated from scattering cross sections at each wavelength by summing contributions from all coupled modes supported by the cluster.

3 Nanostructure assembly and structural characterization

50 nm gold core particles were functionalized with 5'-disulfide-terminated oligonucleotide b. 20 nm silver satellite particles were functionalized with a 5'-thiolated oligonucleotide (b^*defe^*g-s) partially hybridized to a 3'-thiolated oligonucleotide (s/s^*) that forms a 10 base pair (bp) duplex spacer (s/s^*) presenting both a 3'- and a

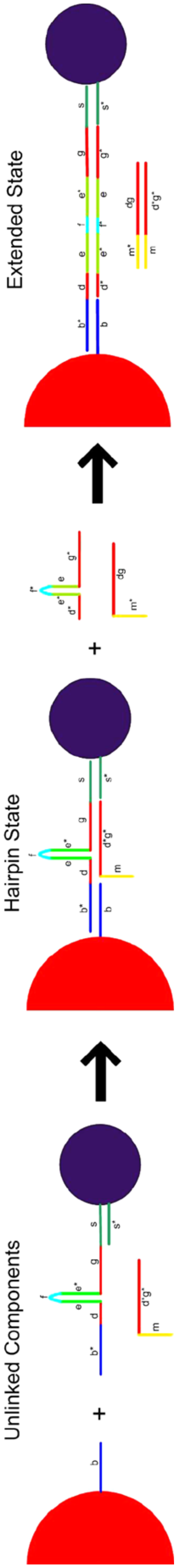

Fig. 3 Assembly of a DNA nanostructure tether in the hairpin state and reconfiguration of the tether into an extended state. Satellite particles initially are linked to cores with a short duplex tether that incorporates a hairpin and is stabilized by a hairpin bridging strand m-d^*g^*. Tether is activated by complement, m^*-dg, to the bridging strand and reconfigures upon hybridization with a strand, complementary to the hairpin, that replaces the hairpin bridging strand. Note that, while multiple satellites are tethered to each core, only a single tether and satellite are illustrated for simplicity

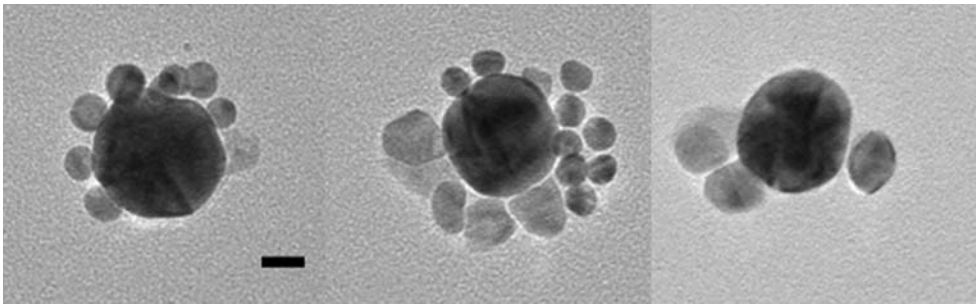

Fig. 4 TEM images of gold core/silver satellite assemblies in the hairpin state. Imaged assemblies display the full range of observed variation in satellite coverage and size. Magnification is identical for all micrographs. Scale bar is 20 nm

5'-thiol to the silver surface. The DNA sequences used in this work are identical to the sequences used to form reconfigurable gold core/gold satellite assemblies, but with the addition of the A_{10} 'spacer', s, to the $b^{*}defe^{*}g$ satellite strand and the inclusion of thiolated T_{10}, s^{*}. The satellite strand is predisposed to form a 24 base hairpin–loop secondary structure composed of a 10 base pair stem (ee^{*}) and a T_4 loop (f). Functionalized cores and satellites were assembled into core–satellite assemblies by combining satellites and cores in a 45:1 ratio in the presence of a hairpin bridging strand (m-$d^{*}g^{*}$). The bridging strand is composed of an 18 base recognition sequence ($d^{*}g^{*}$) complementary to the d and g sequences of the satellite strand, and an 8 base toehold sequence (m) incorporated to facilitate strand replacement. Replacement was performed by introducing a strand (m^{*}-dg) complementary to the toehold and to the hairpin bridging strand and a 42 base recognition strand ($d^{*}e^{*}f^{*}eg^{*}$) that completes the 54 base pair double helix linker. These five strands form a reconfigurable core–satellite tether with two stable conformations: a compact state in which 30 base pairs ($bd^{*}g^{*}$ with complement) control core–satellite separation while 24 bases (efe^{*}) are sequestered within a hairpin–loop formation, and an extended state in which the hairpin is hybridized and incorporated in a 54 base pair tether ($bd^{*}e^{*}f^{*}eg^{*}$ with complement), Fig. 3. Core–satellite separation, thus, is controlled by double helical DNA structures, both of which are much shorter than the persistence length of duplex DNA [33].

Satellite coverage (number of satellite particles per core particle) and assembly yield (fraction of total assemblies composed of satellites on a single-core) were measured by imaging dried assemblies using transmission electron microscopy (TEM). While interparticle separation in desiccated samples is not representative of interparticle separation in hydrated samples [34], TEM images, Fig. 4, provide a direct measure of satellite coverage. Satellite coverage and assembly yield were assumed to be invariant to assembly reconfiguration on the basis of extensive imaging of assemblies composed of 50 nm gold cores and either 13 nm [28] or 20 nm gold satellites (see Supplementary Material), samples that displayed variations in mean coverage between the hairpin and extended states of less than 5%. Coverage in the hairpin state was 6.3 ± 4.2 satellites per core and yield was 87% based upon a sample size of 15 imaged assemblies.

4 Characterization of plasmonic properties

Elastic scattering spectra at a scattering angle of approximately 90° were collected using a custom scattering spectrometer. To insure stability of the assemblies and for consistency with prior measurements of assemblies composed of gold satellites on gold cores, scattering spectra were collected without separating core–satellite assemblies from unbound 'satellites'. Scattering in the spectral region of the silver band was dominated by scattering from dispersed 'satellite' particles (peak scattering intensity of 300 k photons per second; 7-fold excess of dispersed relative to bound particles) and, following preliminary measurements, was not collected. Despite the frequency offset between silver (maximum intensity at 425 nm) and gold (maximum intensity at 545 nm) plasmon bands, heterogeneous broadening of the silver band resulted in overlap with the homogeneously broad gold band. Because of the silver band's high intensity, the red tail of the silver band contributed non-negligibly to scattering at the bluer wavelengths within the gold plasmon band and possibly resulted in a few nm offset of the maximum intensity from the gold band center. Spectra of assemblies in each state were corrected for dilution ($<5\%$) and compared with spectra of dispersed cores and satellites, Fig. 5, upper panel. Resonant scattering from core–satellite assemblies in the hairpin state displayed a $\sim$30% increase in intensity and a 12 nm red-shift of the plasmon band relative to that of dispersed particles. Reconfiguration of the assemblies from the compact hairpin to the extended state resulted in a $\sim$3 nm blue-shift and a $\sim$5% decrease in scattering intensity. On the basis of invariance in yield and satellite coverage to tether transformation observed in assemblies composed of identical 50 nm gold cores and 20 nm gold satellites (sample size: 100 assemblies in each state, see Supplementary Material), differences detected in the scattering spectrum following introduction of the tether transformation strands were interpreted as following from reconfiguration of tethers within existing assemblies. The observed modulation of the core plasmon resonance in the gold core/silver satellite structures was similar to that observed previously in reconfigurable gold core/gold satellite assemblies [28]; following assembly of the compact structure, scattering became more intense and peaked at longer wavelength, whereas, following reconfiguration, scattering became less intense and the resonance less red.

In order to clarify the relationship between the observed perturbation of the gold core plasmon resonance and variations in the core–satellite geometry associated with tether reconfiguration, scattering spectra were simulated for contracted and expanded core–satellite geometries consistent with tethers in the hairpin and extended states. Simulations were performed using an electrodynamic T-matrix coupled multipole method [29] that provides a fully converged description of the delocalized modes supported by a cluster of spherical particles. Scattering simulations were performed using a structural model consisting of a single 50 nm gold core surrounded by 6 evenly spaced 20 nm satellite particles, where the satellite coverage was selected to correspond to the mean number of satellites imaged per core. Based upon prior small-angle X-ray scattering measurements of nearest neighbor distances in both amorphous and crystalline DNA-linked gold particle materials, core–satellite separation was estimated from the number of base pairs in the duplex linker using a 0.25 nm per base pair coefficient [34, 35], and an additional 1.5 nm to account for the unpaired A_{10} spacer on the core strand [34]. Therefore, core–satellite edge-to-edge distance was estimated to be 11.5 nm in the hairpin state (40 bp) and 17.5 nm in the extended state (64 bp). Simulated spectra for assemblies with core–satellite separations of 11.5 and 17.5 nm are illustrated in Fig. 5, lower panel, along with the spectrum of an isolated core particle. Simulated intensities are presented as efficiencies, defined here as equal to the scattering cross section normalized by the geometric cross section of the core. Simulated spectra display distance-dependent coupling similar to the tether state-dependent coupling observed in experiment. Comparison of the spectra simulated for the nominal core–satellite structures and cores revealed perturbations of the gold plasmon that were larger for satellite 'assembly' than for 'reconfiguration' of the linker. Simulated shift in peak position and change in peak intensity associated with change in core–satellite separation were 4 nm and 10%, respectively. Close correlation between observed and simulated plasmon perturbations provided additional support for the hypothesis that tether reconfiguration was driving plasmon perturbation.

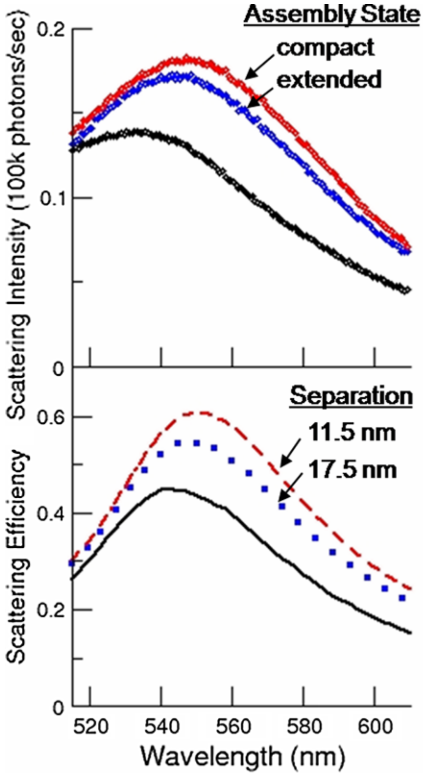

Fig. 5 Scattering spectra and simulated spectra of dispersed particles and core–satellite assemblies. *Top panel*: Ensemble scattering spectra of unlinked particles (*black*) and core–satellite assemblies in hairpin (*red*) and extended (*blue*) states. *Bottom panel*: simulated scattering spectra of 50 nm core (*black*, *solid line*) and core–satellite assemblies with 11.5 nm (*red*, *dashed line*) and 17.5 nm (*blue*, *dotted line*) core–satellite separation (*lower panel*). Simulated scattering cross sections are normalized by the geometric cross section of the core particle

Interestingly, the plasmon perturbations displayed by the binary assemblies are strongly reminiscent of perturbations observed previously in analogous structures composed of gold satellites and cores. Whereas the gold satellites used in the gold-only structures were smaller and assembled in greater numbers at somewhat shorter core–satellite separations because of the absence of a double helical A_{10}–T_{10} anchor, their assembly and subsequent repositioning led to variations in the gold plasmon qualitatively similar to those displayed by the binary structures described here. The qualitative similarity in the perturbations of the gold core plasmon upon coupling to particles of like and unlike (silver) composition is a manifestation of the similar effect on particle plasmon resonance of both coupling to like particles and exposure to polarizable media. The bulk susceptibilities of silver and gold are such that spherical 20 nm silver particles support a low loss dipolar surface plasmon at a frequency higher than that of a gold core. The silver particles, therefore, are polarizable without a phase lag at the lower frequency of the gold core resonance, and their assembly leads to red-shifting of the core resonance through the same mechanism as underlies shifting of particles embedded in transparent dielectric media [6–10]. Red shifting of a gold nanoparticle surface plasmon resonance in the presence of non-resonant metal nano-particulate media has been observed previously in aggregates of gold and silver particles and in gold particles assembled on aggregated silver colloid [12, 36, 37]. In addition to being red-shifted in response to silver satellite assembly, the gold core band is enhanced. Gold particle plasmon enhancement is infrequently observed when red shifting occurs in conjunction with interparticle coupling, because uncontrolled particle aggregation leads to damping of the plasmon band. However, enhancement in conjunction with red shifting was observed originally for spherical gold nanoparticle plasmons red-shifted by dielectric media [4, 38]. Our oligonucleotide tethered core satellite structures composed of gold [28] provide an unusual example of controlled coupling and thus of enhanced scattering correlated with red-shifting. As expected, band intensity was positively correlated with red shift, a correlation consistent with the longer lifetime of plasmons at lower frequencies where interband absorption is less. For core-satellite structure plasmons that are reddest when separations are small, the positive correlation of intensity and red-shift means that the more compact satellite structures are stronger scatterers than the more loosely tethered, larger, structures composed of the same nanoparticles. For the all gold particle structures, we hypothesized that closer coupling of the core and satellites contributed to the increased strength of the oscillator and scattering enhancement thus was greater than that determined by bulk properties at the peak position. However, the enhancement of the gold core band observed here upon assembly of a silver satellite shell may be simply correlated with the frequency dependent susceptibility of gold.

5 Effect of core and satellite composition on plasmon coupling

Having observed that the gold plasmon band can be modulated similarly by coupling with nanoparticles of like [28] and unlike composition, we performed a series of simulations designed to investigate this phenomenon in core–satellite assemblies of a specified geometry. To investigate the dependence of core–satellite coupling on the distribution of gold and silver components, scattering spectra were calculated for a series of core–satellite assemblies with one variable structural parameter and various compositional assignments. Coupling was investigated in assemblies consisting of a single 50 nm core surrounded by twenty evenly spaced 13 nm satellite particles at several core–satellite separations. The structural model was selected to correspond as closely as possible to the structure of the most monodisperse and highly ordered core–satellite structures we have characterized. The structure of recently reported gold core/gold satellite assemblies was selected because high satellite coverage and low satellite size dispersity contributed to consistency of the plasmon properties with structural models that assumed even distribution of identical particles about the core [28].

In order to compare the effects of gold and silver satellite assembly upon a gold core, scattering from assembly structures with core–satellite separations of 5 nm, 10 nm, and 15 nm were simulated using the fully electrodynamic coupled multipole method used to validate the structural model, Fig. 6. These separations were chosen in order to investigate core–satellite geometries in which core and satellite coupling varied from strong to weak. Spectra from gold core/gold satellite assemblies display a single resonance, while spectra from the gold core/silver satellite assemblies display two distinct plasmon bands, a silver resonance at ∼400 nm and a gold resonance at ∼550 nm. Gold band scattering for structures with either gold or silver satellites increases and red-shifts as core–satellite separation is decreased. For a change in separation of 15 to 5 nm, the red-shift in gold peak position is significantly larger (20 nm shift) for gold core structures with gold satellites than for structures with silver satellites (12 nm shift). Interestingly, however, for the particular geometry selected, the silver satellite plasmon displays negligible perturbation as a function of satellite separation from the gold core. The result may be a fortuitous balance of enhancement associated with increased silver particle coupling and damping associated with losses to the core. The spectroscopic signature of core–satellite modulation is clearly illustrated in difference spectra, evaluated here by subtracting spectra of weakly coupled structures (10 or 15 nm separation) from the spectra simulated for the most compact structure (5 nm separation), Fig. 6, lower panels. For structures of both compositions, spectral modulation associated with forming a strongly coupled compact structure is significant regardless of the starting structure, if coupling in the starting structure is weak. The extent of plasmon modulation, thus, depends most strongly on the strength of the coupling in the compact state. For the structures simulated here, with identical satellite size and number, it appears that modulation of core–satellite separation in gold core/gold satellite assemblies results in somewhat larger shifts than in gold/ silver assemblies. From the difference spectra it is apparent that a ratio of red and blue offset scattering intensities (i.e. 580 and 540 nm for the gold core/gold satellite structures simulated here) could be used as a metric to detect changes in interparticle separation. Alternatively, in a binary gold core/silver satellite assembly, the stability of the assembly could be monitored using the invariant silver band, while molecularly driven changes in core–satellite separation were detected as shifts of the gold band.

To determine whether the sensitivity of the gold, but not the silver, plasmon to changes in core–satellite separation carries over to structures with alternative distributions of gold and silver components, spectra were calculated for analogous structures with a silver core. Scattering spectra of assemblies with core–satellite separations of 5 nm, 10 nm,

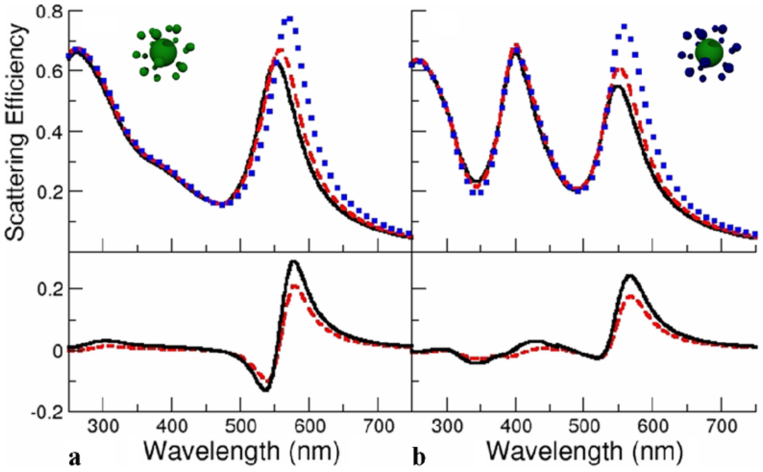

Fig. 6 Simulated scattering spectra for core–satellite structures assembled around a gold core. Structures consist of a 50 nm gold core surrounded by 20 evenly spaced 13 nm gold (**a**) or silver (**b**) satellite particles located 5 nm (*blue*, *dotted*), 10 nm (*red*, *dashed*), or 15 nm (*black*, *solid*) from the core, and corresponding difference spectra of compact (5 nm separation) relative to extended (10 nm, 15 nm separation) states

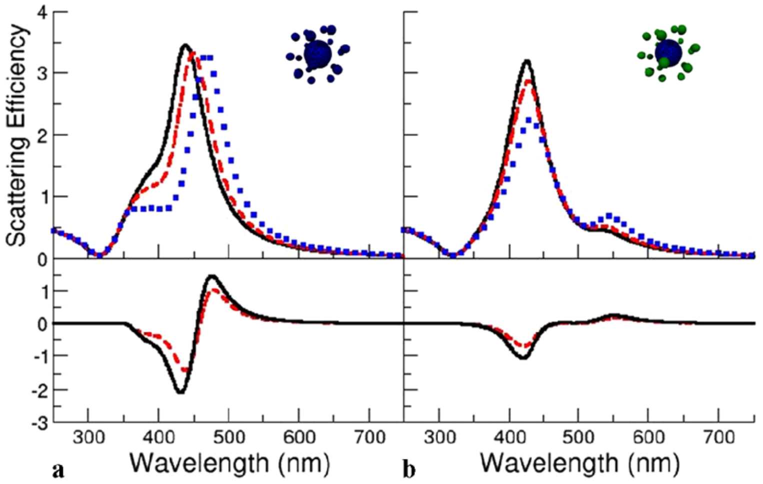

Fig. 7 Simulated scattering spectra for core satellite structures assembled around a silver core. Structures consist of a 50 nm silver core surrounded by 20 evenly spaced 13 nm silver (**a**) or gold (**b**) satellite particles located 5 nm (*blue*, *dotted*), 10 nm (*red*, *dashed*), or 15 nm (*black*, *solid*) from the core, and corresponding difference spectra of compact (5 nm separation) relative to extended (10 nm, 15 nm separation) states. The scale of the lower panel y-axis is reduced by a factor of 1.9

and 15 nm were simulated, Fig. 7. Decreasing core–satellite separation for assemblies with both gold and silver satellites leads to significant, but different, variations in silver plasmon scattering. Whereas increased interaction with gold satellites leads to significant damping (∼30%) of the silver scattering and a small resonance shift (∼5 nm), coupling with silver satellites results primarily in a large resonance shift (∼30 nm). To clarify the quantitative differences in response to interparticle coupling within the selected geometry, simulated difference spectra were generated by subtracting spectra calculated for the more expanded geometries from the spectrum of an assembly with the most compact geometry, Fig. 7, lower panels. The shift associated with coupling within the silver core/silver satellite structure is consistent with expectations of like particle interactions where assemblies of like particles support delocalized red-shifted plasmons analogous to the red-shifted delocalized plasmons supported by larger single particles. The damping of the silver core in the presence of gold satellites is consistent with expectations based upon the lossiness of gold at blue wavelengths, while the absence of significant shifting of the silver core in the presence of gold satellites is a manifestation of the limited polarizability of the gold particles at frequencies above that of the gold particle plasmon. Damping of the localized silver plasmon in the presence of gold has been observed in experiment, both by reduction of gold on colloidal silver [40] and through nanoparticle assembly [12, 36, 37]. Thus the effect of satellites of different compositions and resonance frequencies on a high frequency silver particle resonance displays a greater material dependence than is displayed by satellites of different compositions on the plasmon resonance of a gold core particle whose resonant frequency is close to or less than that of the various satellites considered. This is in contrast to the results for interactions of gold or silver satellites with a gold core, in which either satellite type is polarizable at the core resonance frequency and capable of reducing the core resonance frequency. Particularly noteworthy is the magnitude of the damping displayed by the silver core plasmon in the presence of gold satellites, given the insensitivity of the silver satellite plasmon to association with a gold core. Clearly the response of a binary assembly to interparticle coupling is highly dependent not only upon interparticle separation, but also upon distribution of the component materials within the

Table 1 Character of plasmon perturbations associated with assembly

Components\Band	Silver band	Gold band
Au satellites on Au core		Enhancement, red-shift
Ag satellites on Au core	Negligible[a]	Enhancement, red-shift
Ag satellites on Ag core	Red-shift	
Au satellites on Ag core	Damping	Enhancement

[a] Possibly a consequence of cancellation of intra-shell and core–shell effects specific to the details of the particular structure considered here

assembly. From the positions of maxima and minima in the difference spectra, it appears that reconfiguration of silver core/gold satellite assemblies could be monitored by comparing intensities of silver and gold plasmon scattering.

In summary, on the basis of the scattering properties of the core–satellite structures simulated here, the manifestation of core–satellite coupling appears to depend upon both the plasmonic properties of the components and their distribution within the structure, Table 1. Whereas both silver and gold particles can red-shift a gold particle resonance and a gold resonance will be enhanced when red-shifted from frequencies at which intrinsic losses are high, the damping effect of gold on silver, while also an intrinsic effect, may be offset or eliminated by competing enhancing factors. Thus, the effect upon a silver plasmon of interaction with gold appears to be dependent upon geometry, i.e. the distribution of like and unlike particles. For example, increased coupling of silver satellites with a gold core negligibly affects the silver plasmon; however, increased coupling of gold satellites with a silver core significantly damps the silver plasmon. This geometric dependence of the spectral response to gold–silver coupling warrants additional investigation.

6 Conclusion

In recent years, there have been several reports of the formation of binary metal nanoparticle structures and networks assemblies [12, 22, 37, 41]. The reports document characteristic spectral properties of gold and silver nanoparticle coupling that include support of multiple resonances, damping of the silver band, and red-shifting or enhancement of the gold band. Here we have demonstrated molecularly controlled modulation of binary gold and silver surface plasmon coupling in assemblies of well-defined geometry and interparticle separation. The work was enabled by a new method for formation of stable DNA–silver particle conjugates that takes advantage of the increased affinity of multiple thiols for the silver particle surface. We have formed gold core/silver satellite assemblies, and, through molecularly driven modulation of the gold/silver interparticle separation, have demonstrated that the DNA–silver conjugates exhibit similar functionality to conjugates composed of gold. Plasmon coupling in binary silver and gold particle assemblies leads to perturbation of the low frequency gold core plasmon that is remarkably similar to that observed previously in core–satellite assemblies composed exclusively of gold. From further investigation through simulation of coupling in structures of like geometry but alternative distributions of gold and silver components, the delocalized plasmons supported by the binary structures are found to have different sensitivities to details in component arrangement. Specifically, for the core–satellite structures studied here, gold plasmons appear to be systematically red-shifted by silver particles, whereas plasmons supported by silver particles are differentially sensitive to gold particles according to whether the silver particle is in a core position or a satellite shell. A deeper understanding of the geometric dependence of non-resonant coupling will follow from future investigations of a broader range of structures. Nevertheless, binary metal nanostructures that support multiple plasmon bands can be expected to display a richer set of spectral signatures sensitive to geometry than may be achievable with assemblies of like components.

Acknowledgements The support of the NSF (DMR-0706397) is gratefully acknowledged. D.S.S acknowledges support from an NSF IGERT Grant (DGE-0221632). This work was partially supported by Grant W911NF-05-1-0466 from the Army Research Office and Grant CCF-0650083 from the NSF to T.H.L.

References

1. U. Kreibig, M. Vollmer, *Optical Properties of Metal Clusters* (Springer, Berlin, 1995)
2. J.J. Mock, M. Barbie, D.R. Smith, D.A. Schultz, S. Schultz, J. Chem. Phys. **116**, 6755 (2002)
3. K.L. Kelly, E. Coronado, L.L. Zhao, G.C. Schatz, J. Phys. Chem. B **107**, 668 (2003)
4. C.A. Mirkin, R.L. Letsinger, R.C. Mucic, J.J. Storhoff, Nature **382**, 607 (1996)
5. K.H. Su, Q.H. Wei, X. Zhang, J.J. Mock, D.R. Smith, S. Schultz, Nano Lett. **3**, 1087 (2003)
6. S. Underwood, P. Mulvaney, Langmuir **10**, 3427 (1994)
7. T.R. Jensen, M.L. Duval, K.L. Kelly, A.A. Lazarides, G.C. Schatz, R.P. Van Duyne, J. Phys. Chem. B **103**, 9846 (1999)
8. J.J. Mock, D.R. Smith, S. Schultz, Nano Lett. **3**, 485 (2003)
9. R. Bukasov, J.S. Shumaker-Parry, Nano Lett. **7**, 1113 (2007)
10. E.M. Larsson, J. Alegret, M. Kall, D.S. Sutherland, Nano Lett. **7**, 1256 (2007)
11. A.P. Alivisatos, K.P. Johnsson, X.G. Peng, T.E. Wilson, C.J. Loweth, M.P. Bruchez, P.G. Schultz, Nature **382**, 609 (1996)
12. I. Tokareva, E. Hutter, J. Am. Chem. Soc. **126**, 15784 (2004)
13. Z. Wang, R. Levy, D.G. Fernig, M. Brust, Bioconjugate Chem. **16**, 497 (2005)
14. S.J. Park, A.A. Lazarides, C.A. Mirkin, R.L. Letsinger, Angew. Chem. Int. Ed. **40**, 2909 (2001)
15. K.K. Caswell, J.N. Wilson, U.H.F. Bunz, C.J. Murphy, J. Am. Chem. Soc. **125**, 13914 (2003)
16. L.R. Hirsch, J.B. Jackson, A. Lee, N.J. Halas, J. West, Anal. Chem. **75**, 2377 (2003)

17. C.S. Yun, G.A. Khitrov, D.E. Vergona, N.O. Reich, G.F. Strouse, J. Am. Chem. Soc. **124**, 7644 (2002)
18. C. Sonnichsen, B.M. Reinhard, J. Liphardt, A.P. Alivisatos, Nat. Biotechnol. **23**, 741 (2005)
19. A.A. Lazarides, G.C. Schatz, J. Phys. Chem. B **104**, 460 (2000)
20. T. Herricks, J.Y. Chen, Y.N. Xia, Nano Lett. **4**, 2367 (2004)
21. D.B. Pedersen, S. Wang, J. Phys. Chem. C **111**, 17493 (2007)
22. B.C. Vidal, T.C. Deivaraj, J. Yang, H.P. Too, G.M. Chow, L.M. Gan, J.Y. Lee, New J. Chem. **29**, 812 (2005)
23. T.A. Taton, *Current Protocols in Nucleic Acid Chemistry*, 12.2.1–12.2.12 (Wiley, New York, 2002)
24. Y.D. Yin, Z.Y. Li, Z.Y. Zhong, B. Gates, Y.N. Xia, S. Venkateswaran, J. Mat. Chem. **12**, 522 (2002)
25. J.S. Lee, A.K.R. Lytton-Jean, S.J. Hurst, C.A. Mirkin, Nano Lett. **7**, 2112 (2007)
26. D.G. Thompson, A. Enright, K. Faulds, W.E. Smith, D. Graham, Anal. Chem. **80**, 2805 (2008)
27. J.J. Storhoff, A.A. Lazarides, R.C. Mucic, C.A. Mirkin, R.L. Letsinger, G.C. Schatz, J. Am. Chem. Soc. **122**, 4640 (2000)
28. D.S. Sebba, J.J. Mock, D.R. Smith, T.H. LaBean, A.A. Lazarides, Nano Lett. **8**, 1803 (2008)
29. D.W. Mackowski, J. Opt. Soc. Am. A: Opt. Image Sci. Vis. **11**, 2851 (1994)
30. P.B. Johnson, R.W. Christy, Phys. Rev. B **6**, 4370 (1972)
31. E.D. Palik, *Handbook of Optical Constants of Solids* (Academic, New York, 1985)
32. W.A. Kraus, G.C. Schatz, J. Chem. Phys. **79**, 6130 (1983)
33. V.A. Bloomfield, D.M. Crothers, I. Tinoco Jr., *Nucleic Acids: Structures, Properties, and Functions* (University Science Books, Sausalito, 2000)
34. S.J. Park, A.A. Lazarides, J.J. Storhoff, L. Pesce, C.A. Mirkin, Phys. Chem. B **108**, 12375 (2004)
35. H.D. Hill, R.J. Macfarlane, A.J. Senesi, B. Lee, S.Y. Park, C.A. Mirkin, Nano Lett. **8**, 2341 (2008)
36. C.D. Keating, K.K. Kovaleski, M.J. Natan, Phys. Chem. B **102**, 9414 (1998)
37. A.M. Kalsin, B. Kowalczyk, S.K. Smoukov, R. Klajn, B.A. Grzybowski, J. Am. Chem. Soc. **128**, 15046 (2006)
38. B.M. Reinhard, M. Siu, H. Agarwal, A.P. Alivisatos, J. Liphardt, Nano Lett. **5**, 2246 (2005)
39. P. Mulvaney, M. Giersig, A. Henglein, J. Phys. Chem. **97**, 7061 (1993)
40. P. Mulvaney, M. Giersig, A. Henglein, J. Phys. Chem. **97**, 7061 (1993)
41. C.D. Keating, K.M. Kovaleski, M.J. Natan, J. Phys. Chem. B **102**, 9404 (1998)